Journal of Applied Geophysics 229 (2024) 105490

Contents lists available at ScienceDirect

Journal of Applied Geophysics

journal homepage: www.elsevier.com/locate/jappgeo

Minimum entropy constrained cooperative inversion of electrical resistivity, seismic and magnetic data

Anton H. Ziegon *, Marc S. Boxberg, Florian M. Wagner

Geophysical Imaging and Monitoring (GIM), RWTH Aachen University, Wüllnerstraße 2, 52062 Aachen, Germany

ARTICLE INFO

Keywords:
Applied geophysics
Imaging
Joint inversion
Inverse theory
Entropy constraints

ABSTRACT

Geophysical methods are widely used to gather information about the subsurface as they are non-intrusive and comparably cheap. However, the solution to the geophysical inverse problem is inherently non-unique, which introduces considerable uncertainties. As a partial remedy to this problem, independently acquired geophysical data sets can be jointly inverted to reduce ambiguities in the resulting multi-physical subsurface images. A novel cooperative inversion approach with joint minimum entropy constraints is used to create more consistent multi-physical images with sharper boundaries with respect to the single-method inversions. Here, this approach is implemented in an open-source software and its applicability on electrical resistivity tomography (ERT), seismic refraction tomography (SRT), and magnetic data is investigated. A synthetic 2D ERT and SRT data study is used to demonstrate the approach and to investigate the influence of the governing parameters. The findings showcase the advantage of the joint minimum entropy (JME) stabilizer over separate, conventional smoothness-constrained inversions. The method is then used to analyze field data from Rockeskyller Kopf, Germany. 3D ERT and magnetic data are combined and the results confirm the expected volcanic diatreme structure with improved details. The multi-physical images of both methods are consistent in some regions, as similar boundaries are produced in the resulting models. Because of its sensitivity to hydrologic conditions in the subsurface, observations suggest that the ERT method senses different structures than the magnetic method. These structures in the ERT result do not seem to be enforced on the magnetic susceptibility distribution, showcasing the flexibility of the approach. Both investigations outline the importance of a suitable parameter and reference model selection for the performance of the approach and suggest careful parameter tests prior to the joint inversion. With proper settings, the JME inversion is a promising tool for geophysical imaging, however, this work also identifies some objectives for future studies and additional research to explore and optimize the method.

1. Introduction

Geophysical methods are widely used to gather information about the subsurface, as they are non-intrusive, comparably cheap while providing lots of flexibility in the survey design (Kearey et al., 2002). They have been proven to be an invaluable tool for a multitude of applications ranging from resource exploration (Dentith and Mudge, 2014; Kana et al., 2015; Kearey et al., 2002) and process monitoring (Klotzsche et al., 2019; Steiner et al., 2021) to building integrity tests (Maack et al., 2022; Niederleithinger et al., 2016). However, geophysical methods have the drawback that they are generally prone to ambiguities, meaning there are several geophysical models that explain the data within their uncertainty arising from the inherent non-uniqueness of the inverse problem (Menke, 2018; Zhdanov, 2015). Noise and human errors during data acquisition in addition to assumptions and simplifications in the modelling and inversion frameworks introduce further uncertainties that could lead to a degradation of the reliability of the results (Kearey et al., 2002). To counteract ambiguity it is common practice to combine different geophysical methods in a joint interpretation. Even though different geophysical methods sense the same subsurface features, the resulting images might indicate different structures. To address this issue, several approaches have been developed that couple several geophysical methods during the data inversion rather than in the interpretation phase. These joint inversion schemes are able to produce more consistent geophysical models as ambiguities during the data inversion are reduced by the enforcement of petrophysical or

* Corresponding author.
E-mail address: anton.ziegon@rwth-aachen.de (A.H. Ziegon).

https://doi.org/10.1016/j.jappgeo.2024.105490
Received 21 December 2023; Received in revised form 14 May 2024; Accepted 10 August 2024
Available online 20 August 2024

structural relationships (e.g. (Gallardo, 2007; Gallardo and Meju, 2004; Gallardo et al., 2005; Haber and Gazit, 2013; Moorkamp et al., 2011; Moorkamp et al., 2016; Skibbe et al., 2021; Steiner et al., 2021)). This coupling of different geophysical methods is generally non-trivial and requires complex physical and mathematical formulations along with additional computational power, however, due to the advances in high-performance computing in the recent decade, the latter is no longer the main obstacle. Haber and Holtzman Gazit (Haber and Gazit, 2013), Moorkamp et al. (Moorkamp et al., 2016) and Wagner and Uhlemann (Wagner and Uhlemann, 2021) give an extensive overview of the most common joint inversion approaches with a multitude of synthetic and field data examples.

One of the latest advances in the field of geophysical joint inversion is presented by Zhdanov et al. (Zhdanov et al., 2022), who introduce a structural coupling based on joint minimum entropy (JME) formulations. The authors demonstrate the new scheme in the context of magnetic and gravity data for large scale mineral exploration purposes with very promising results as these multi-physical images show significant improvements towards structural similarity as well as image sharpness. A validation of this approach in a more local context using seismic, electric or electromagnetic methods is yet to be presented. Therefore, this work aims to validate this approach using a synthetic data study including electrical resistivity tomography (ERT) and seismic refraction tomography (SRT) data as well as a field data study of ERT and magnetic data.

2. Theory and methods

The main part of this theory section is based on Zhdanov et al. (Zhdanov et al., 2022), who introduced the concept of joint minimum entropy constraints.

2.1. Entropy on model space

In the field of information theory, the term entropy can be understood as the level of uncertainty or information of a system of random variables (Shannon, 1948). The concept of entropy can also be translated to the model space which is subject of a geophysical data inversion. Before performing the entropy calculations, model parameters need to be normalized. This is essential with regard to the joint entropy constraints as it ensures comparability between different geophysical model spaces. A logarithmic normalization is performed as follows:

$$\boldsymbol{m}^{i}_{\text{norm}} = \frac{ln\mathbf{m}^{i} - min(ln\mathbf{m}^{i})}{max(ln\mathbf{m}^{i}) - min(ln\mathbf{m}^{i}) + \beta} \tag{1}$$

Here, $\boldsymbol{m}^i$ refers to the model parameters of the method i and β to a numerical stabilizer. Note that in the following equation, subscripts and superscripts are dropped such that normalized model parameters are presented as $\boldsymbol{m}$. The entropy on the model space can then be expressed through (Haber and Gazit, 2013; Zhdanov et al., 2022):

$$H(\boldsymbol{m}) = -\int_{\Omega} p_m(\boldsymbol{m}(\boldsymbol{r})\,)\; ln p_m(\boldsymbol{m}(\boldsymbol{r})\,)\; d\boldsymbol{r} \tag{2}$$

Ω represents the entire modelling space, namely a 2D or 3D mesh, and $p_m(\boldsymbol{m}(\boldsymbol{r})\,)$ a pseudo-probability density function acting on the model space which is a function of the cell position $\boldsymbol{r}$. Zhdanov et al. (Zhdanov et al., 2022) propose the following formulation:

$$p_m(\boldsymbol{m}(\boldsymbol{r})\,) = \frac{|\boldsymbol{m}(\boldsymbol{r}) - \boldsymbol{m}_{\text{ref}}(\boldsymbol{r})\,|^{q} + \beta}{Q_m} \tag{3}$$

$$\text{where} \quad Q_m = \int_{\Omega} |\boldsymbol{m}(\boldsymbol{r}) - \boldsymbol{m}_{\text{ref}}(\boldsymbol{r})\,|^{q} + \beta \; d\boldsymbol{r} \tag{4}$$

As seen in Eq. 3, the pseudo-probability density function is based on model contrasts between a set of normalized model parameters and some normalized reference model to the power of order q. The normalization factor Q_m ensures that p_m has unity norm and the numerical stabilizer β removes the singularity for models identical to the reference model. Note that Eq. 1, 3 and 4 use the same numerical stabilizer. Its effect can be neglected if it is chosen much smaller than the model parameters; in this study the parameter was kept fixed at 10^{-10}.

2.2. Joint entropy on model space

The pseudo-probability density function can be modified such that Eq. 2 represents the joint entropy of several models. For M geophysical methods, the following expression is emerging (Zhdanov et al., 2022):

$$p_{\text{Jm}} = \frac{\sum_{i=1}^{M}\left(w_m^{(i)}\left|\boldsymbol{m}^{(i)}(\boldsymbol{r}) - \boldsymbol{m}^{(i)}_{\text{ref}}(\boldsymbol{r})\,\right|^{q} + \beta\right)}{Q_{\text{qJME}}} = \sum_{i=1}^{M} p^{(i)}_{\text{Jm}} \tag{5}$$

$$\text{where} \quad Q_{\text{Jm}} = \int_{\Omega}\sum_{i=1}^{M}\left(w_m^{(i)}\left|\boldsymbol{m}^{(i)}(\boldsymbol{r}) - \boldsymbol{m}^{(i)}_{\text{ref}}(\boldsymbol{r})\,\right|^{q} + \beta\right) d\boldsymbol{r} \tag{6}$$

It can be seen that the joint entropy is calculated through the sum of model contrasts over all methods in each model cell. The contrasts are weighted with respect to each other through the method weighting factor $w_m^{(i)}$, which allows better control over the structural coupling with regard to a joint inversion. Q_{Jm} ensures a unit norm similar to the single method case (Eq. 3). $p^{(i)}_{\text{Jm}}$ represents the contribution of each method i to the joint entropy pseudo-probability density function. Note that Eq. 5 and 6 equal Eq. 3 and 4 for $M = 1$ and $w_m = 1$. To illustrate the meaning of Eq. 2, 5 and 6, consider the two model scenarios in Fig. 1. Shown are two models, $\boldsymbol{m}^{(1)}$ and $\boldsymbol{m}^{(2)}$, with identical block anomalies that are increasingy shifted apart from each other or smoothed. The corresponding pseudo-probability density function p_{Jm} and the resulting entropy value H can be extracted from the bottom row. The reference model $\boldsymbol{m}^{(i)}_{\text{ref}}$ is chosen to be a homogeneous model that resembles the background of both models. Therefore, contrasts with respect to the reference model occur in the location of the respective anomalies. This results in a large probability, i.e. large p_{Jm}, for a model anomaly to exist in this region. A comparison of the four scenarios illustrates that smoothing or shifting increases the area that significantly contributes to p_{Jm} which ultimately increases the joint entropy H of the models. The shifted models indicate that areas, where the anomalies of both models are overlapping, have the largest p_{Jm} values, which ultimately suggests that a joint anomaly is most likely to occur in this region. These observations justify the joint minimum entropy as a suitable constraint in a joint inversion algorithm as a minimization of the joint entropy H promotes sharp anomalies, i.e. model contrasts with respect to the reference model, in similar regions. Further visualization of this concept will be provided at the end of this section.

2.3. Pseudo-quadratic joint minimum entropy stabilizers

As the goal is to minimize the joint entropy, the corresponding expression (Eq. 2, 5) can be plugged into the joint objective functional φ_{JME} of the joint inversion instance to be minimized. The problem is that these entropy expressions are non quadratic and therefore cannot be used in conventional quadratic optimization schemes such as the Gauss-Newton method (Loke and Dahlin, 2002). Zhdanov et al. (Zhdanov et al., 2022) introduce a pseudo-quadratic stabilizer S_{JME} that is used as a regularization term in the objective functional weighted by the regularization parameter λ:

$$\varphi_{\mathrm{JME}}\left(\boldsymbol{m}^{(1)},\boldsymbol{m}^{(2)},\ldots,\boldsymbol{m}^{(M)}\right) = \sum_{i=1}^{M}\varphi_d^{(i)} + \lambda S_{\mathrm{JME}} = \sum_{i=1}^{M}\varphi_d^{(i)} + \sum_{i=1}^{M}\lambda^{(i)}\left(\boldsymbol{m}^{(i)} - \boldsymbol{m}_{\mathrm{ref}}^{(i)}\right)^T \boldsymbol{W}_e^{(i)T}\,\boldsymbol{W}_e^{(i)}\left(\boldsymbol{m}^{(i)} - \boldsymbol{m}_{\mathrm{ref}}^{(i)}\right) \tag{7}$$

$\varphi_d^{(i)}$ represents the data misfit functional of method i which is presented in more detail in Zhdanov (Zhdanov, 2015) and Menke (Menke, 2018). The stabilizer has a quadratic form and consists of model contrasts and a diagonal matrix $\boldsymbol{W}_e^{(i)}$ with method specific model weights $\omega_{\mathrm{JME}}^{(i)}$ on its diagonal, that will introduce variable damping on the model parameters during the inversion. The weights are calculated as shown in Eq. 8:

$$\omega_{\mathrm{JME}}^{(i)}(\boldsymbol{r}) = \left[\frac{p_{\mathrm{Jm}}^{(i)}}{\left|\boldsymbol{m}^{(i)}(\boldsymbol{r}) - \boldsymbol{m}_{\mathrm{ref}}^{(i)}(\boldsymbol{r})\right|^2 + \beta} ln\frac{1}{p_{\mathrm{Jm}}}\right]^{\frac{1}{2}} \tag{8}$$

Eq. 7 and 8 indicate that the functionals related to a method i can be separated. This leads to a cooperative inversion scheme that requires a recalculation of the method specific model weights after each iteration. The exact derivation of this expression can be found in Zhdanov et al. (Zhdanov et al., 2022). $\omega_{\mathrm{JME}}^{(i)}$ is also referred to as joint minimum entropy (JME) weights. In case of only one method, they are referred to as minimum entropy (ME) weights. It is important to mention that the discretization of the continuous integrals of Eq. 2 and 6 produces a factor related to the cell size. This can be neglected for regular grids, however, for many applications unstructured meshing is more suitable, in which case the distribution of the cell sizes accross the modelling domain strongly affects the model weighting (see Fig. 2). Introducing meshing related structure in the structural constraint might result in inversion outputs, i.e. physical parameter distributions, that resemble meshing structures rather than data-based subsurface features. As this is not desired within this study, the cell size factor will be neglected such that Eq. 8 holds.

The approach is implemented within the open-source geophysical modelling and inversion library pyGIMLi (Rücker et al., 2017). The implemented Gauss-Newton inversion framework allows to extend the diagonal matrix $\boldsymbol{W}_e^{(i)}$ by an additional first-order smoothing operator, which results in smoothing in combination with damping within the model regularization. The smoothing constraints in the extended model weighting matrix are weighted with a smoothing factor $a^{(i)}$ for each method i. The smoothing operator is weighted by a times the mean of $\omega_{\mathrm{JME}}^{(i)}$ and therefore $a = 0$ will reduce to pure damping in the inversion.

It is also important to mention that the implementation allows to use the starting models of the inversion frameworks as the reference models as well as a splitting of starting and reference models. The latter was proven to be more beneficial for the SRT inversion as demonstrated in section 3.

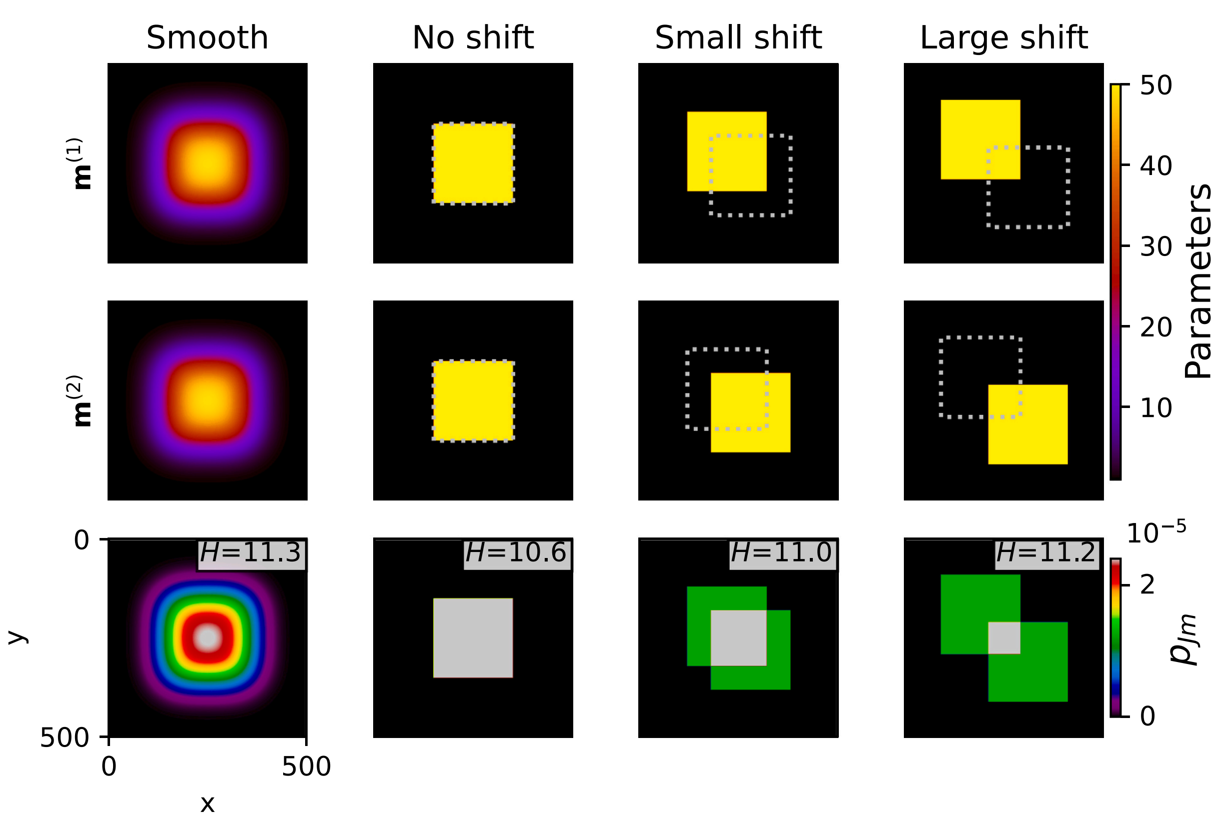

Fig. 1. Illustrations of joint entropy (H) based pseudo-probability functions p_{Jm}.
Top and middle row refer to $\boldsymbol{m}^{(1)}$ and $\boldsymbol{m}^{(2)}$, respectively, and bottom row shows the resulting p_{Jm} distribution with the joint entropy value. The superimposed dotted line indicates the location of the anomaly in the other model. Note that the the largest p_{Jm} values occurs in regions where the anomalies overlap and that the joint entropy H is minimized for sharp anomalies in identical regions.

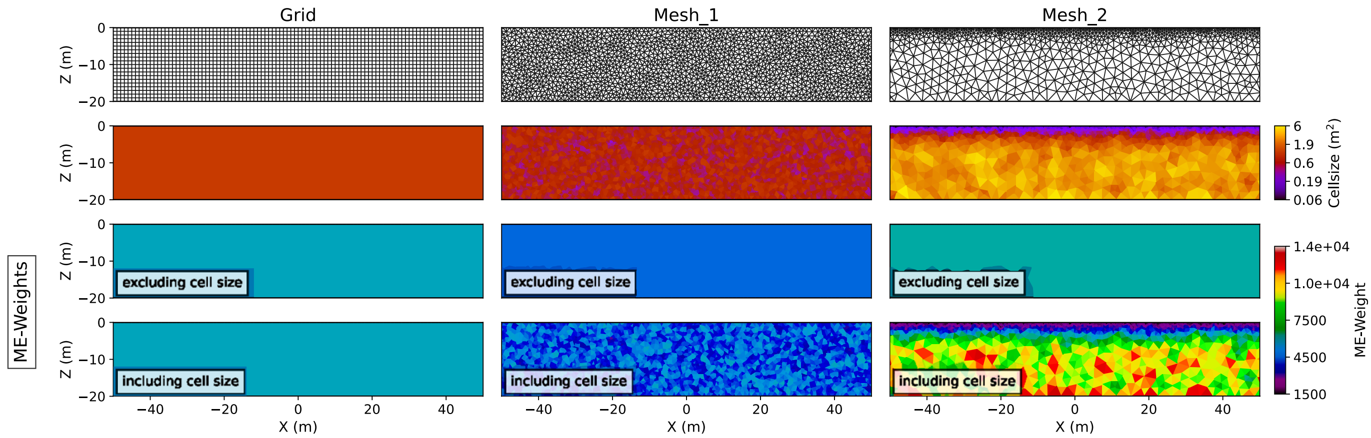

Fig. 2. Illustration of cell size effects in the ME-weights.
The columns are corresponding to a regular grid (left), a fine triangular mesh (middle) and a highly irregular mesh (right). The discretization with corresponding cell sizes are shown in the first two rows, while the weights of the homogeneous models are shown in the bottom rows. Note that the reference model equals the homogeneous model. Inclusion of cell sizes introduces meshing related structure into the weights which is not desirable in this study.

2.4. Illustration of model weights

Consider the simple 2D models presented in Fig. 3, namely a homogeneous model, a gradient model and a block model. As seen in the governing equations (Eq. 5, 6, 8), the weight calculation requires a reference model. For this simple demonstration, the homogeneous model is set as the reference model for all three models. The bottom row of Fig. 3 shows the resulting ME weights of the corresponding models. As expected, the homogeneous model has homogeneous ME weights as it is identical with the reference model everywhere. The gradient and block model show higher weights in regions where they are equal or close to the homogeneous reference model and lower weights where strong model contrasts occur. Since the entropy weighting is within the frame of damping, this means that regions of the model that are close to the reference model are stronger damped towards the reference model and vice versa. Therefore, the ME weighting leads to the development of fewer yet stronger anomalies rather in contrast to smaller ones, which coincides with a decreased model entropy.

Now consider two different methods that are used to reconstruct different physical model parameters. Fig. 4 presents two different models that show a rectangular anomaly of different strength. To better showcase the effects of the JME weights along with the method weighting the anomalies are slightly shifted with respect to each other. Note that the reference model is a homogeneous model with the value of the background of both models. The second row presents the JME weights of model 1 and model 2 without method weighting. It can be seen that in addition to the region of the anomaly of the method itself also the anomaly of the other method appears with comparably low weights. This means that during the joint inversion model changes with respect to the reference model are promoted where any of the methods already have a strong contrast. The lowest weights can be found in the region where the anomalies are overlapping meaning that parameter changes are strongly encouraged in that region. Therefore, this will produce similar structure in both models during the cooperative inversion. The bottom two rows present the JME weights with a stronger method weighting on either model 1 or model 2. It can be observed that the anomaly of the higher weighted method is more dominant in the resulting model weights. This will cause the weaker weighted model to become more similar to the higher weighted. However, with increasing method weighting, this rather flexible exchange of structural information will lead to a strong structural constraint on the weaker weighted method such that the exchange of structural information is increasingly lopsided. A big risk of this is that possible inversion artefacts, like ray artefacts or other features created by noisy data, are enforced on another method making the inversion results rather worse than better. Therefore, it is suggested to use this method weighting with caution and only with small weighting factors to avoid running into these issues related to structural enforcement. Note that the method weighting factor can also be used to help one method converge better as a higher weighted method has more freedom to fit the data.

3. Synthetic data study

For this synthetic 2D model study, the ERT and SRT methods are considered. Therefore, a velocity model as well as an electrical resistivity model are constructed (Fig. 5). Both models show the same two anomalous bodies, namely a square on the left and a circle on the right. However, to make it more realistic the models are also differing in some aspects. The background resistivity is chosen to be constant at 700 Ωm, while the velocity background shows a high velocity layer (4000 m s − 1) underneath a low velocity layer (500 m s − 1). This is also beneficial to improve the ray coverage in the region of the anomalies during the

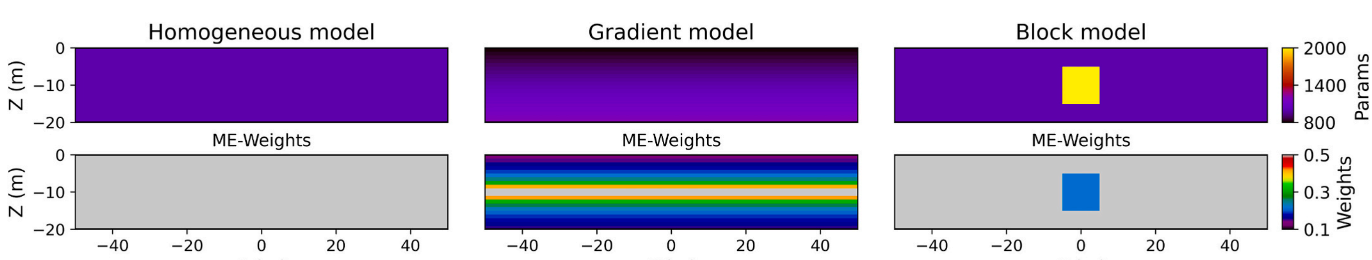

Fig. 3. Illustration of ME weights (bottom row) of three simple 2D models (top row).
The reference model for all three models was set to the homogeneous model. Note that the following parameters were fixed: $\beta = 10^{-10}$, $q = 1$.

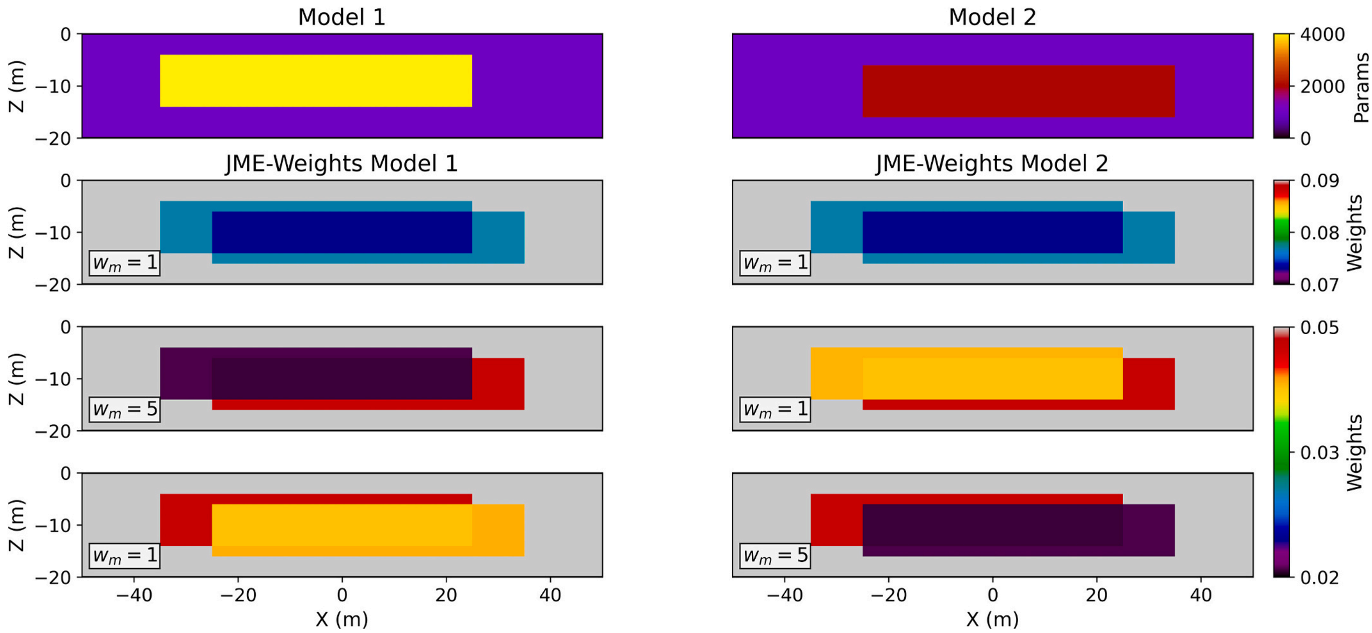

Fig. 4. Example of joint minimum entropy weights for simple 2D models.
The rows correspond to related JME weights. The method weighting factors for both models are indicated by the text box in bottom left corner of each model weights plot. The model reference resembles the background of both models. Note that the following parameters were fixed: $\beta = 10^{-10}$, $q = 1$.

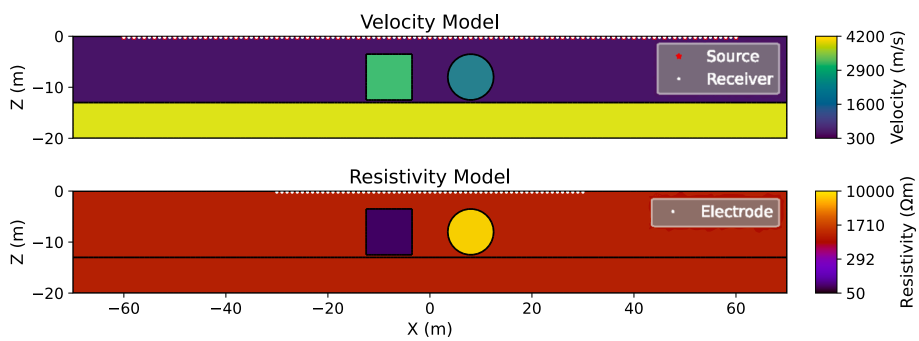

Fig. 5. Seismic velocity model (top) and electrical resistivity model (bottom) that are used for the synthetic SRT and ERT data generation in pyGIMLi (Rücker et al., 2017).

forward calculation of the seismic traveltimes as the bottom layer is a good refractor (Kearey et al., 2002). Furthermore, it allows to investigate if the seismic data will enforce this layered structure in the ERT result during the joint inversion.

Fig. 5 also shows the source and receiver locations used for the SRT data generation as well as all electrode locations for the ERT dipole-dipole survey. The acquisition spread of the SRT method is chosen to be twice as long as the electrode spread for the ERT method to improve the experimental design of the study (Kearey et al., 2002). Note that additional noise is superimposed on the synthetic data to make the scenario more realistic. The ERT noise reaches up to 2.5% of the simulated data and SRT measurements are affected by an absolute error or 0.001 ms. In the following sections only the part of the model between −30 m and 30 m are discussed as this is the region of the model domain that hosts the anomalies and that has good data coverage in both methods. The starting models are a homogeneous model with the mean value of the simulated apparent resistivities, namely 706 Ωm, for the ERT method and a vertical gradient model ranging from 500 m s−1 to 4200 m s−1 for the SRT method. For both methods homogeneous reference models of 700 Ωm and 500 m s−1 are selected, respectively.

3.1. Sensitivity study

Before multi-method inversions are performed, the effects of the regularization parameter λ and the smoothing factor a are investigated. The parameter tests are only presented for the SRT method as the parameter effects are better illustrated than for the ERT method. Note that the numerical stabilizer is kept fixed at a small value of $\beta = 10^{-10}$ for all following ME and JME inversions in this work as it was proven to have no significant influence on the outcome and is only required to avoid division by zero in Eq. 1, 3, 5, and 8.

Standalone ME inversion results of the synthetic SRT data are presented in Fig. 6. Note that these results are obtained for an order of q = 1. The final inversion results for three different λ (columns) and three different a (rows) are presented. In the first row, results with no smoothing, and therefore pure damping, are presented. They show very noisy results as the images do not indicate any clear structures. With increasing regularization, less high-velocity model cells emerge in the velocity images. For the highest λ, it seems like high-velocity cells are focused in regions of high ray coverage, and therefore resembling ray artefacts. Better results are obtained for additional smoothing. However, it can be seen that the SRT method generally requires strong smoothing to obtain reasonable velocity models. A possible reason for that might

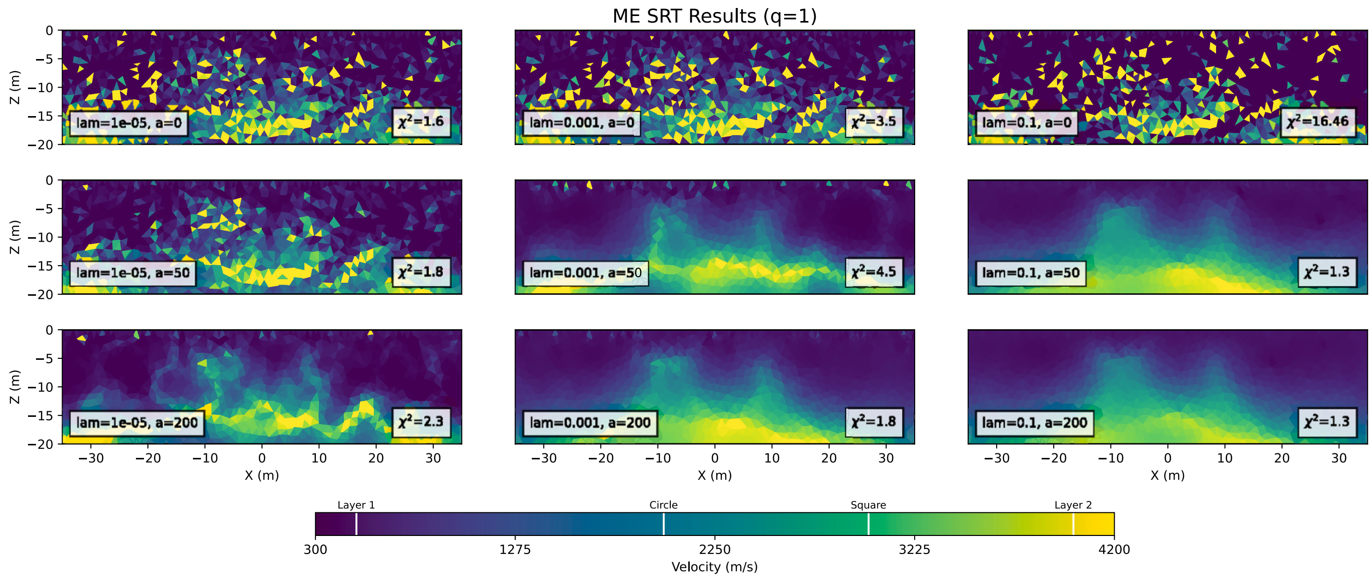

Fig. 6. Standalone SRT ME Results for three different smoothing factors a and three different regularization parameters. $a = 0$ refers to a model regularization of pure damping which is not beneficial for SRT inversions. Note that following parameters were fixed: λ, $q = 1$ and $\beta = 10^{-10}$.

be, that the entropy constraints collapse high-velocity structures to smaller, even higher velocity structures that bundle many ray paths. Therefore, smoothing is needed to counteract this behavior and obtain reasonable models. The test reveals that λ and a are related as the smoothing increases not only with a but also with λ for a smoothing factor $a > 0$. The results for $\lambda = 10^{-5}$ are generally not very clear and worse than the results for higher λ values. Therefore, a higher regularization parameter between 10^{-3} and 10^{-1} is suggested in this scenario together with a smoothing factor between 50 and 200. This parameter

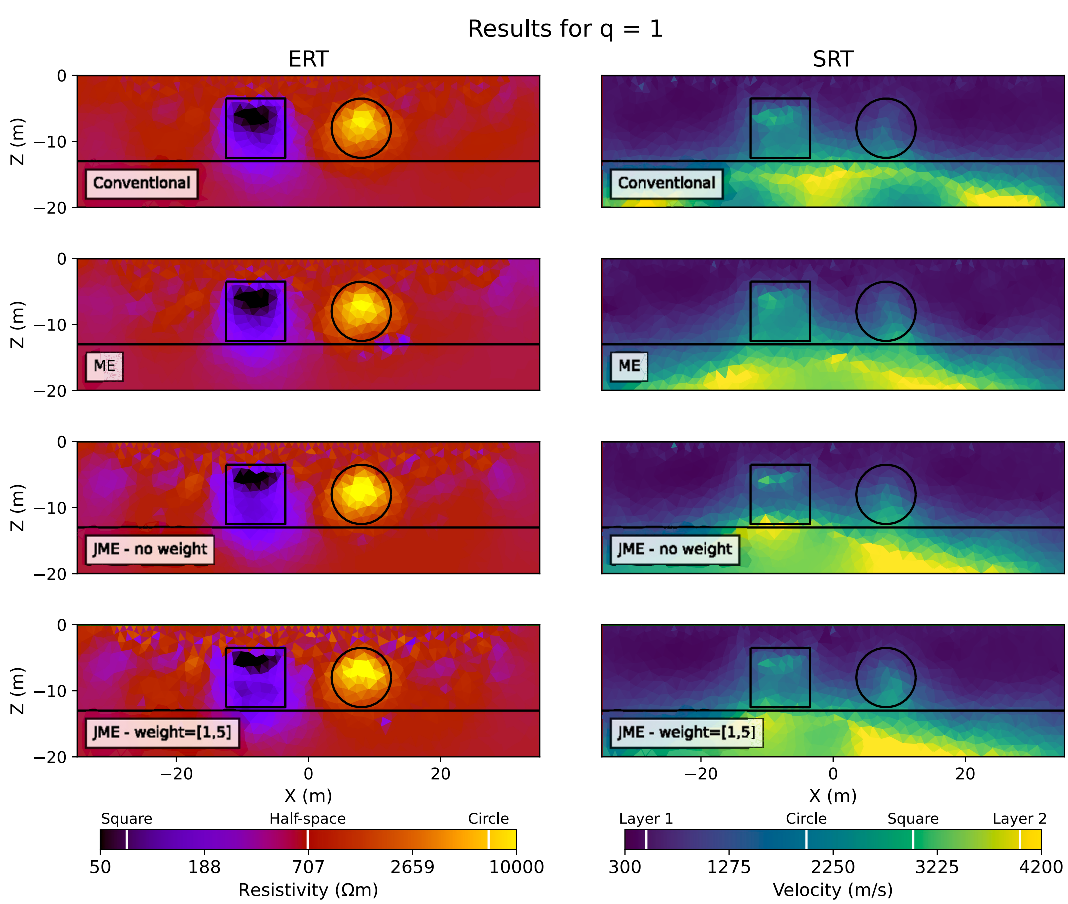

Fig. 7. Comparison of conventional inversion, standalone ME inversion as well as unweighted and weighted JME inversion results of ERT and SRT data. Shown are the estimated model parameters of the last iteration. The entropy inversions have the following fixed parameters: $q = 1$, $\beta = 10^{-10}$, $\lambda_{ERT} = 0.003$, $\lambda_{SRT} = 0.05$, $a_{ERT} = 15$, $a_{SRT} = 30$.

range is further confirmed by a relatively good measure of the error weighted data misfit functional, i.e. the root mean square error, χ^2 close to 1. Similar observations can be made when performing the same test on the ERT method as pure damping is not a suitable regularization approach and therefore further justifies the extension of the matrix $\boldsymbol{W}_e^{(i)}$. It is important to mention that the smoothing is counteracting the minimum entropy constraint as no sharp boundaries are produced, however, Fig. 6 indicates that the additional smoothing is necessary to make the approach applicable to the SRT method. Therefore, a should not be chosen too big to erase the positive effects of the entropy constraints.

3.2. Result comparison

Fig. 7 presents a comparison of the velocity and electrical resistivity models obtained from conventional smoothness-constrained inversions, first-order standalone ME inversions and first-order JME inversions. The conventional inversion is able to retrieve the resistivity distribution sufficiently, but it does not fully recover the true velocity model as the bottom layer and the right anomaly are not imaged properly. In contrast to that, the standalone ME SRT inversion result shows a more continuous bottom layer with a slightly more dominant left anomaly and an improved right anomaly. The ERT result shows slight improvements in the imaging of the resistive circle as well as the bottom of the square anomaly, however, it seems to come with the drawback of a less homogeneous background due to the damping nature of the approach.

For the joint inversion an unweighted scenario with method weighting factors of 1 for both methods (third row) and a weighted JME approach with five-times weighting on the SRT inversion (bottom row) are considered. The unweighted JME results show an improvement in the imaging of right anomaly for both methods. Especially in the ERT result the magnitude of the resistivity is more in accordance with the true model and the anomaly appears to be less smoothed. The left conductive anomaly in the resistivity image appears to have two separated zones, namely a highly conductive zone at the top and a less conductive one underneath due to the JME constraints. The SRT result shows little to no improvements of the left anomaly, however, the top appears more dominant, which can be related to the more conductive region in the resistivity image demonstrating the structural coupling.

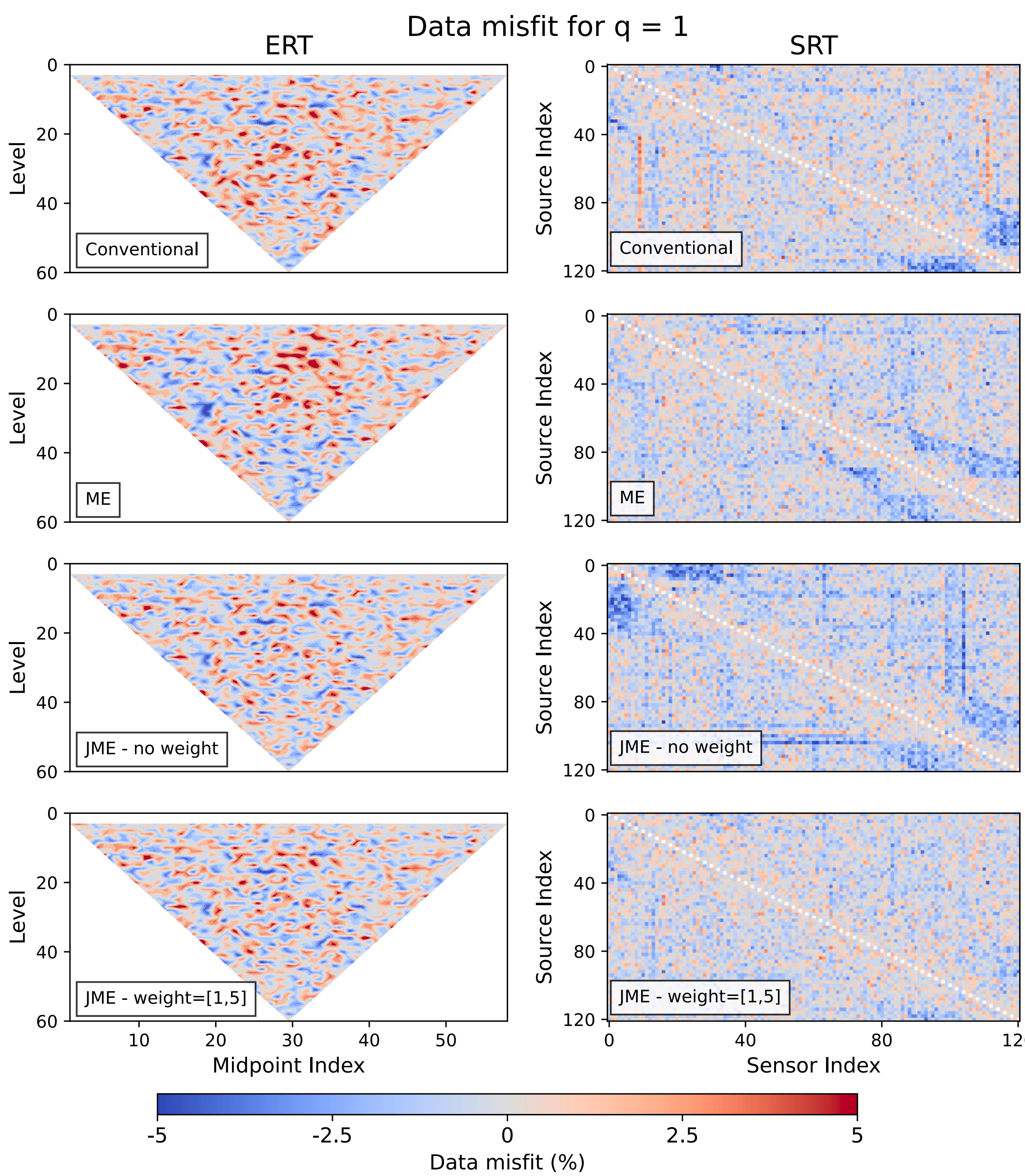

Fig. 8. Resulting data misfit of ERT (left) and SRT (right) inversion results of Fig. 7.

For a higher weighting on the SRT method the left velocity anomaly appears slightly more homogeneous and the right one more dominant. The bottom of the conductive feature is also more conductive, which can be explained through a stronger contribution of the seismic velocity model contrast with respect to the reference model in that region and therefore further illustrates the structural coupling between the methods.

For a proper comparison of the different results the data misfit should be taken into consideration (Fig. 8). The ERT results show very good data fits for all inversions with slight improvements for the coupled inversions. In contrast to that, there are clear differences between the SRT data fits. The fit of the conventional inversion appears to be slightly worse than the standalone ME inversion. The misfit pattern shows a slight elevation for the unweighted JME inversion, however, for stronger weighting on the SRT method the misfit is improved and randomized. These observations and the improved multi-physical models (Fig. 7) indicate the positive effects of the joint inversion on the multi-physical imaging scenario.

The second-order equivalent inversion results, i.e. $q = 2$, are presented in Fig. 9. While the standalone ME inversions show improved models for both methods, the joint inversion results look less promising than their first-order equivalents. The ERT JME results show strong variations close to the surface with slightly worse imaging of both anomalies. The resulting JME velocity models show collapsed high-velocity zones that cause a focusing of the raypaths, something that has already been observed in Fig. 6. These observations indicate that the second-order entropy expressions might be useful for standalone inversions, however, they do not seem to be suitable for the joint inversions. It is important to note that all SRT inversions fail to reconstruct the true velocity model accurate, as the smoothing that is required prohibits the development of sharp boundaries. While the improvements of the JME inversion are minor, they still give valuable insight on the effects of the parameters and the applicability of JME constraints on the SRT method.

3.3. Reference models

As seen in Eq. 5, anomalies are defined in regions where a strong model contrast with respect to the reference model occurs. In the cooperative inversion with the JME constraints, the structural coupling will then be strongest in regions where all methods show a model contrast with respect to their respective reference model. Therefore, the reference models have to be chosen carefully as they have a major influence on the structural coupling. In this section, a JME inversion is performed for the four different reference models for the SRT method, namely the homogeneous reference model and the gradient starting model of the previous subsections as well as a two-layer model resembling the background of the true model and the SRT result of conventional smoothness-constrained inversion (see Fig. 10). Note that the homogeneous 700 Ωm resistivity model is kept as the ERT reference model. The corresponding JME results are presented in Fig. 11. The SRT results show clear differences that can be related to the reference model, as the homogeneous and the two-layer model show improved imaging over the other two reference models. The latter two lack consistency of the bottom layer and fail to recover the signature of the right anomaly. Arguably, the best results are obtained for the two-layer model, as the bottom layer is imaged relatively homogeneous and a comparable strong, isolated signature of the right anomaly is recovered. The ERT

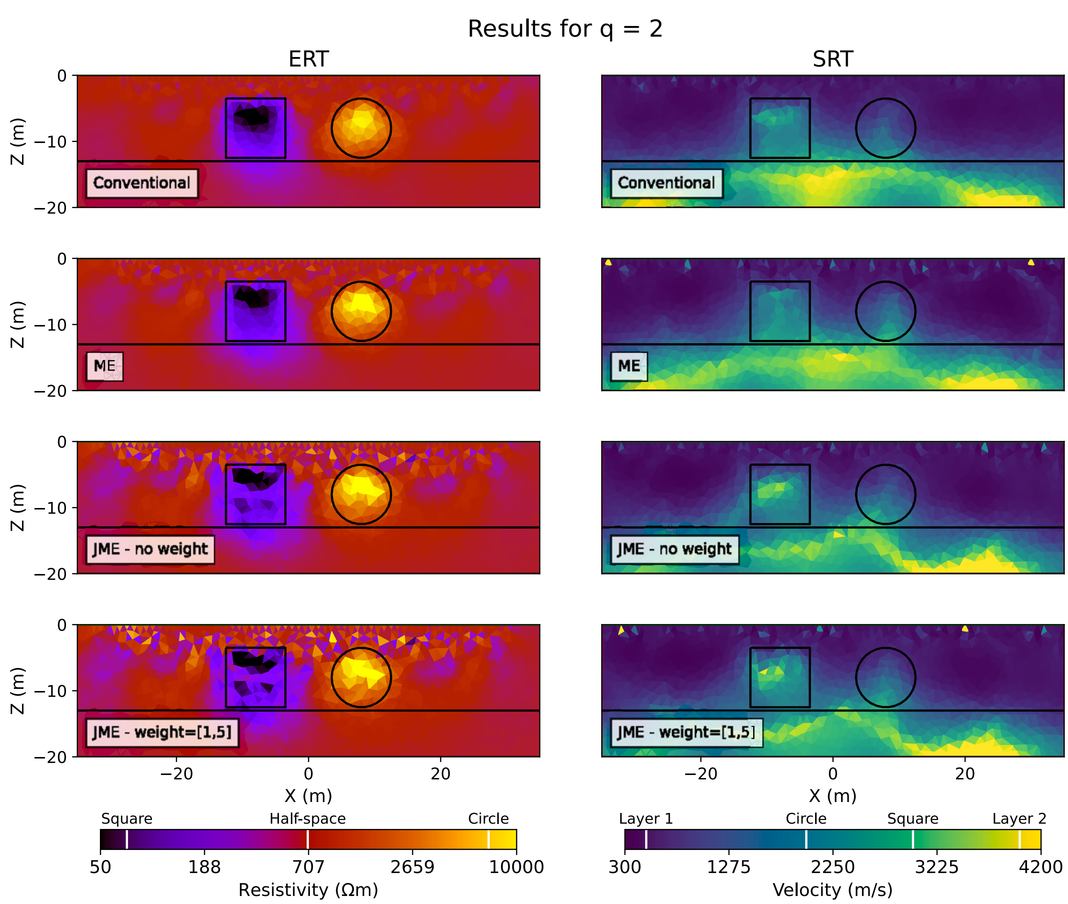

Fig. 9. Comparison of conventional inversion, standalone ME inversion as well as unweighted and weighted JME inversion results of ERT and SRT data. Shown are the estimated model parameters of the last iteration. The entropy inversions have the following fixed parameters: $q = 2$, $\beta = 10^{-10}$, $\lambda_{\mathrm{ERT}} = 0.003$, $\lambda_{\mathrm{SRT}} = 0.05$, $a_{\mathrm{ERT}} = 15$, $a_{\mathrm{SRT}} = 30$.

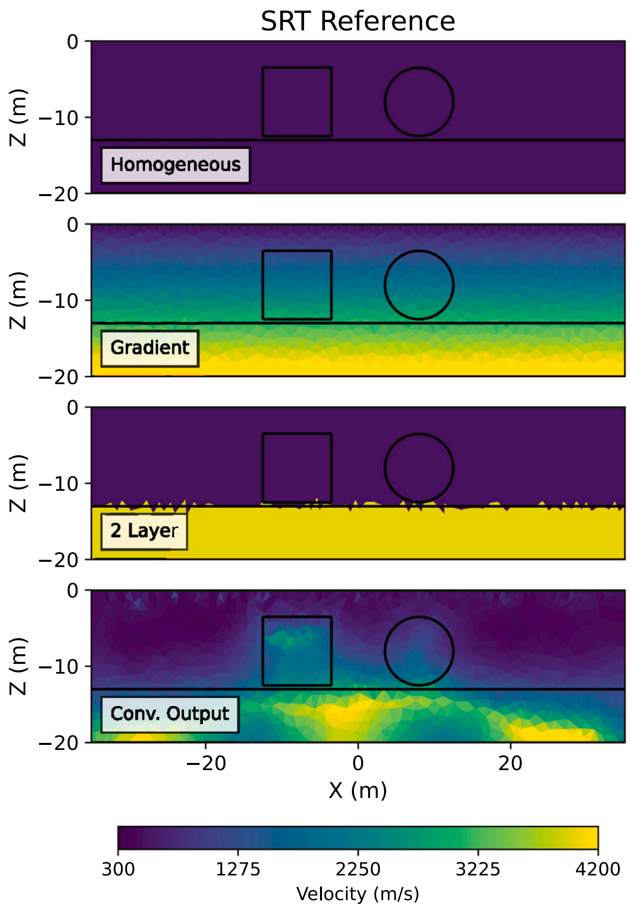

Fig. 10. Different reference models for the SRT inversion.
Considered are a homogeneous, gradient, and two-layer model as well as the conventional inversion output. Note that the homogeneous and gradient models are the reference and starting model of previous inversion, respectively.

results show little differences, however, the bottom of the left anomaly appears stronger for the two-layer SRT reference model. Furthermore, the high resistivity region in the top half of the right anomaly coincides with the isolated velocity signature of the right anomaly showcasing the structural coupling. These results underline the importance of the reference model on the JME inversion output of all methods and they suggest that the two-layer model for the SRT is most beneficial for this specific study. However, due to the smoothing that is required to obtain reasonable models, changes appear relatively subtle and no sharp boundaries along the two anomalies are created. This further suggests that this regularization approach is not as beneficial for the SRT method as demonstrated for potential field methods in Zhdanov et al. (Zhdanov et al., 2022).

The superior behavior of the homogeneous and the two-layer reference model can be explained by considering the model contrasts of reference models with respect to the true models (Fig. 12). In this case, the ERT method has a homogeneous reference model identical to the background and therefore the resistivity model contrasts coincide exactly with the two anomalies. However, in the case of homogeneous, gradient and two-layer SRT reference models, the location of velocity model contrasts change considerably. For two-layer and homogeneous reference models, contrasts are identical with the ERT anomalies, with the latter having an additional anomaly in the bottom layer structure. In contrast to that, the gradient model produces model contrasts predominantly outside the actual square and circle anomalies. As the structural coupling within the JME inversion requires model contrasts to be in the same region, better images are obtained for the homogeneous and two-layer reference models, while the gradient reference model results in a comparably poor seismic velocity distribution. The same can be derived for a reference model like the conventional inversion output, which already includes the seismic velocity features to some degree and is somewhat close to the true model. These observations and thoughts explain why homogeneous and two-layer reference models are preferred over the other two and why the two-layer model shows slight improvements with respect to the homogeneous reference model. Therefore, it can be concluded that the structural coupling does not require a reference models that holds information about shared subsurface features. The opposite is the case as reference models without the shared features will improve the structural coupling between the methods.

It is recommended that the reference model resembles the background as good as possible and should, for example, include prior knowledge of layers or physical property distributions. If no certain prior knowledge is available, homogeneous models are the best choice for the model reference. In case of seismic data inversion, a homogeneous model with a velocity of the uppermost layer is preferred as it can be directly inferred from the observed traveltimes and performs better than the gradient starting model. It might also be possible to extract more sophisticated background models through low-dimensional representations of conventional inversion results, for example a layered reference model. This procedure would further allow to identify possible subsurface features that occur in all multi-physical images, which ultimately guides the choice of the model references. One might argue that the reference model can be neglected, but it is important to recognize that neglecting the reference model in Eq. 3 to 8 is equal to a homogeneous reference model of zero. Such a model is non-physical for velocity or resistivity distributions and therefore is not suitable as a reference model for the ERT and SRT method. However, it can be chosen as the starting and reference model for the magnetic or gravity method since the data can be inverted for susceptibility or density contrasts with respect to the background, which makes the reference model less influential in potential field inversions. This could also be an indication that the approach is more suitable for those methods, as the choice of the reference model can be neglected. Note that the original paper of Zhdanov et al. (Zhdanov et al., 2022) does not discuss implications with regard to the choice different reference models likely due to the their negligible effect on potential field methods such as gravity and magnetics.

4. Field data study: Rockeskyller Kopf, Germany

To further illustrate the approach a field data application is presented in this section. The study site is located in the Westeifel, Germany, (Fig. 13a) near the Rockeskyller Kopf volcanic complex. The goal is to identify a volcanic diatreme structure suspected to be the eruptive source of huge sanidine crystals which are indicating an abnormal volcanism for the region. The host rock is known to be a sandstone (Hopmann, 1914). A first dense magnetic survey revealed a strong total magnetic field anomaly indicating volcanic rocks (Boxberg and Friederich, 2024; Mertes, 1983). For better imaging of the diatreme structure, four ERT lines were acquired, intersecting the central part of the magnetic acquisition geometry (Fig. 13b), which coincides with the center of the magnetic anomaly. Under the assumption that the volcanic rock holds higher electrical resistivities than the surrounding sandstone, the ERT and magnetic method are able to sense the same diatreme structure, which allows to perform a 3D JME inversion of both methods. Using the magnetic method also allows to validate the implementation of the approach as the magnetic ME and JME results should hold similar characteristics compared to the results of Zhdanov et al. (Zhdanov et al., 2022).

In this field study, the reference models are chosen to be equal to the homogeneous starting models of the respective geophysical method. Fig. 14 presents a comparison of the conventional smoothness-constrained inversions alongside the standalone ME and JME

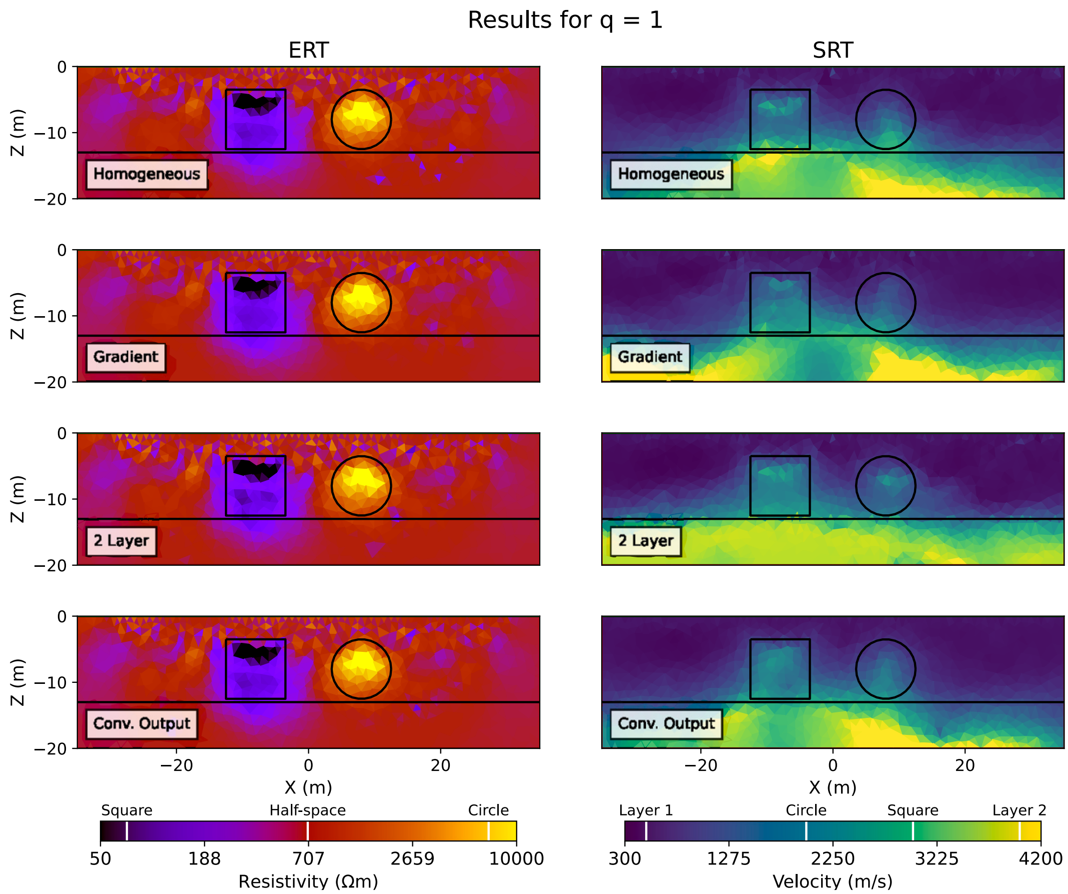

Fig. 11. Comparison of JME inversion results of ERT and SRT data with the four different SRT reference models considered in Fig. 10. Shown are the estimated model parameters of the last iteration.

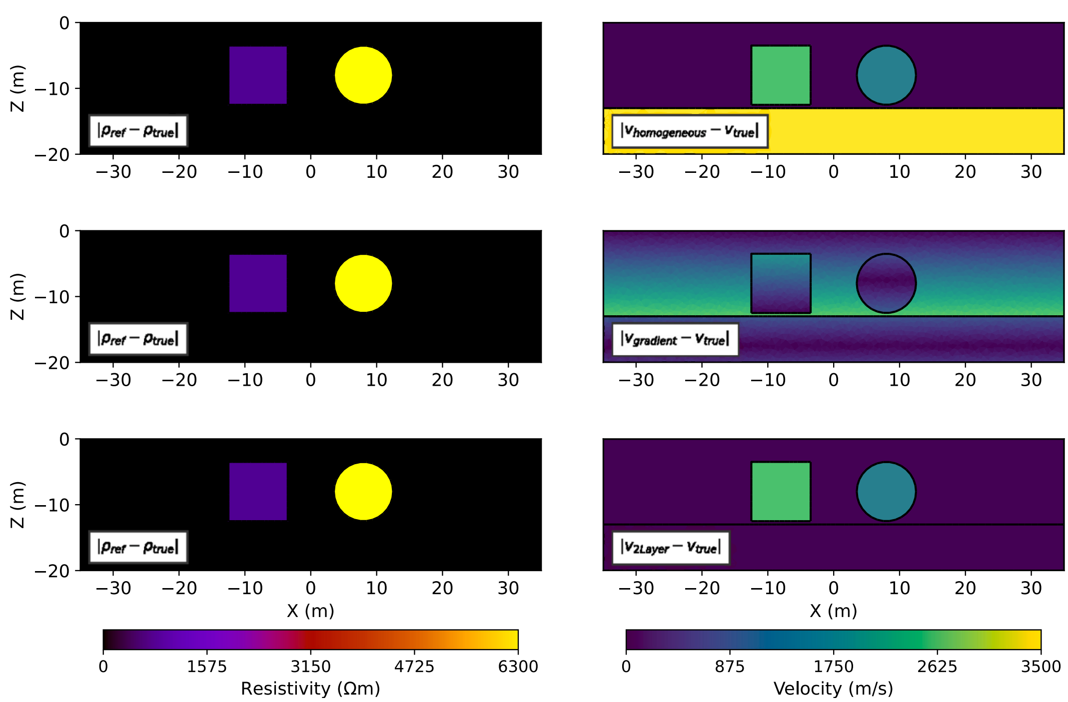

Fig. 12. Comparison of model contrasts of the reference models of the synthetic data study with respect to the true models (Fig. 5). Considered is the homogeneous ERT reference model as well as the homogeneous, gradient and two-layer model reference for the SRT method (Fig. 10). The gradient model is not a suitable reference model as velocity model contrasts do not occur in the same regions as for the resistivity models.

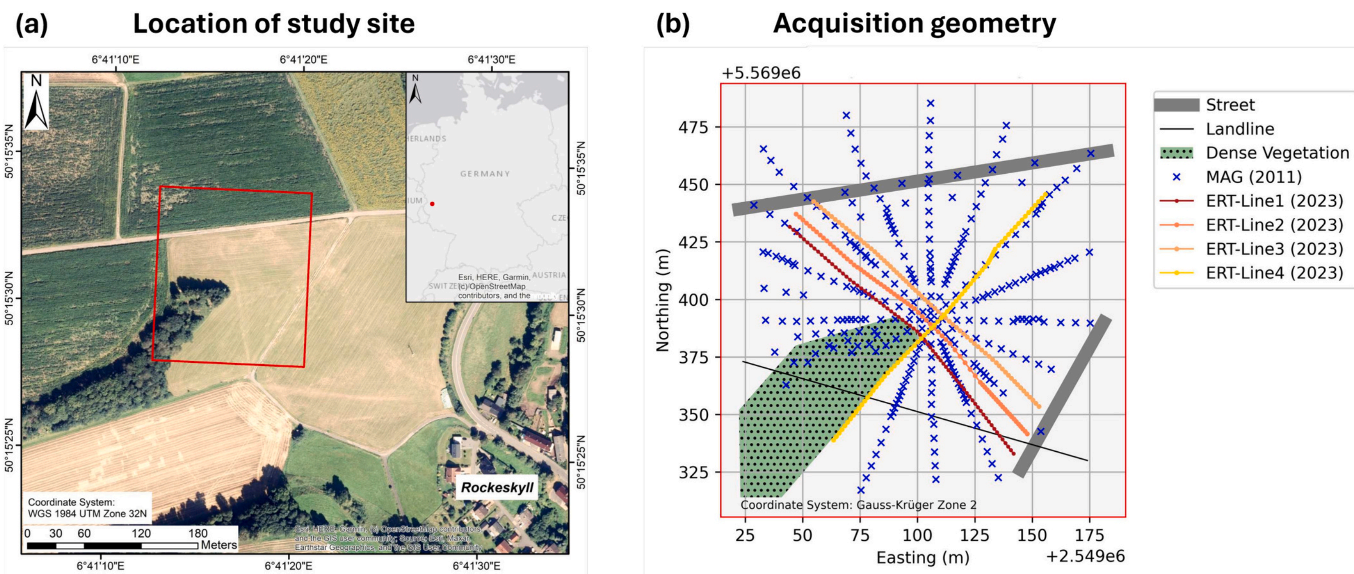

Fig. 13. Maps of the study area (a) and the acquisition geometry (b).
The red dot on the top right map of (a) shows the location of the main map within Germany. The red rectangle indicates the position of (b). (For interpretation of the references to colour in this figure legend, the reader is referred to the web version of this article.)

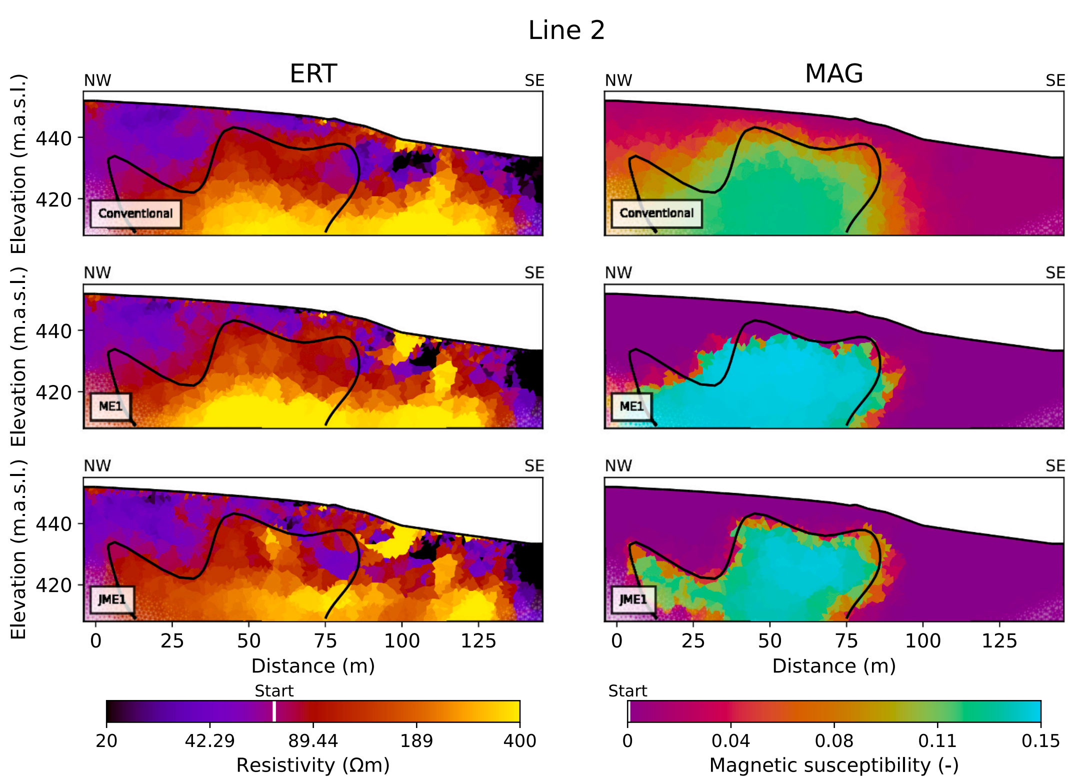

Fig. 14. Comparison of conventional, ME standalone and JME inversion results underneath ERT line 2 (see Fig. 13b).
The black lines outline the magnetic (MAG) anomaly of the JME inversion to better illustrate shared structures. The following parameters are used: q, $\lambda_{\mathrm{ERT}} = 0.005$, $\lambda_{\mathrm{MAG}} = 0.05$, $a_{\mathrm{ERT}} = 35$, $a_{\mathrm{MAG}} = 50$, $w_{\mathrm{m,ERT}} = 10$, $w_{\mathrm{m,MAG}} = 1$ and $\beta = 10^{-10}$.

inversions. Shown is a cross-section through the resulting 3D models underneath ERT Line 2 (Fig. 13b).

The conventional ERT result shows a high-resistive feature at the bottom of the model reaching over 400 Ωm. Towards the southeastern end of the slope relatively strong resistivity variations occur near the surface. The corresponding 3D magnetic inversion result shows a smooth magnetic susceptibility anomaly. The magnitude of the anomaly reaches over 0.1 in its core while the surrounding host rock appears non-magnetic. It is important to mention that the model parameter range had to be limited during the magnetic inversion to avoid obtaining unrealistic susceptibility values and therefore has a large influence on the appearance of the magnetic anomaly. Based on literature and previous investigations in the area, the susceptibility is limited to values between 0 and 0.15 (Lowrie and Fichtner, 2020; Mertes, 1983), which explains the maximum susceptibility contrast that is observed in the anomaly.

The standalone ME result of the ERT method shows a similar structure to the conventional result, however, the magnitudes of the feature appear elevated due to the underlying entropy constraint. In contrast to that, the magnetic result shows major improvements as the anomaly appears as a homogeneous body with a sharp boundary, which illustrates the sparsity constraint of the ME expression. The susceptibility contrast is slightly larger than in the conventional result with 0.15. Note that the diatreme structure is assumed to have a relatively sharp boundary in the magnetic susceptibility distribution instead of a gradual change as the host rock is not expected to be penetrated laterally, which ultimately provides a lateral constraint to the diatreme structure.

The JME results show clear differences to the conventional smoothness-constrained inversion and the standalone ME results. The magnetic anomaly shows a changed shape with respect to the ME results. The boundary of the magnetic susceptibility anomaly is also present in the resistivity image, however, the match between the two different methods is better in the northwestern part than towards the southern end of the slope, where strong resistivity variations occur. The high resistive feature of the ME inversion appears diminished inside the magnetic anomaly and cut off from another high resistive feature on the southern end of the line. It is important to mention that the magnetic anomaly appears less homogeneous, which is probably connected to the changed shape while providing good data fit. Furthermore, the ERT results show comparably strong resistivity variations inside the magnetic anomaly as resistivity increases with depth. Overall, the JME results indicate a clear improvement towards structural similarity as a shared boundary is developed. Considering the corresponding ERT and magnetic data misfits (see Fig. 15), an improvement from conventional to standalone ME inversions can be observed in both methods. However, the JME inversion result indicates slight improvements only in the ERT pseudosections, while magnetic data fits appear slightly worsened. It is important to mention that in the inversion, a stronger weighting was put on the ERT method, which limits the freedom to fit certain structures in the magnetic inversion to some degree, and therefore could explain why increased misfits appear can be observed. These observations once again underline the beneficial influence of the JME inversion on model reconstruction and data fit.

A 3D visualization of the JME results is provided in Fig. 16. The strong magnetic susceptibility anomaly of over 0.1 indicates volcanic rocks and therefore suggests the suspected diatreme structure. The irregular shape of the anomaly is in accordance with the eruptive mechanism that caused parts of the host rock alongside the volcanic rocks to be erupted. Relatively low electrical resistivities at shallow depths and increasing resistivities towards deeper regions, indicated by ERT results, might indicate increasing compaction with depth of erupted volcanics, that partially fell back into the crater. The position of the magnetic anomaly is partly in accordance with the ERT results. A relatively good match between the high susceptibility and higher resistivity regions can be observed in the northwestern part of the suspected diatreme. Towards the southeastern region stronger resistivity variations occur that probably originate from changing hydrologic conditions due to recent rainfalls in the region, that are sensed by the ERT method, but not captured by the total magnetic field measurements of the magnetic method. This ultimately suggests that in the southeastern part the two methods do not sense the same structure, however, the results in Figs. 14 and 16 indicate that these resistivity changes do not influence the magnetic susceptibility distribution in the JME inversion. This demonstrates the flexibility of the approach, which supports shared features while allowing different methods to develop their unique structures throughout the structurally coupled inversion. In conclusion, the JME inversion returns a plausible, consistent multi-physical image that resulted in a detailed interpretation.

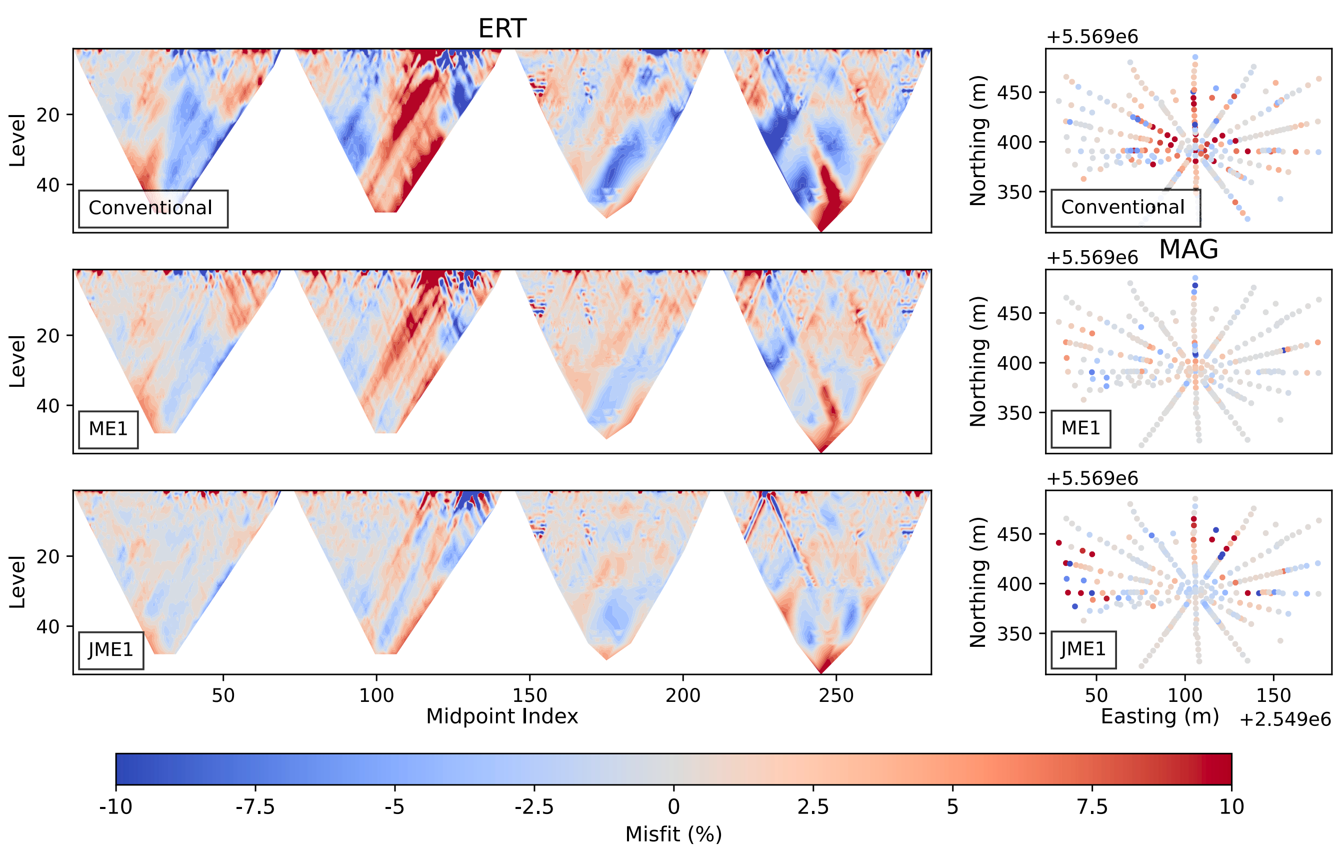

Fig. 15. Resulting data misfit of ERT (left) and magnetic (right) inversion results of Fig. 14.

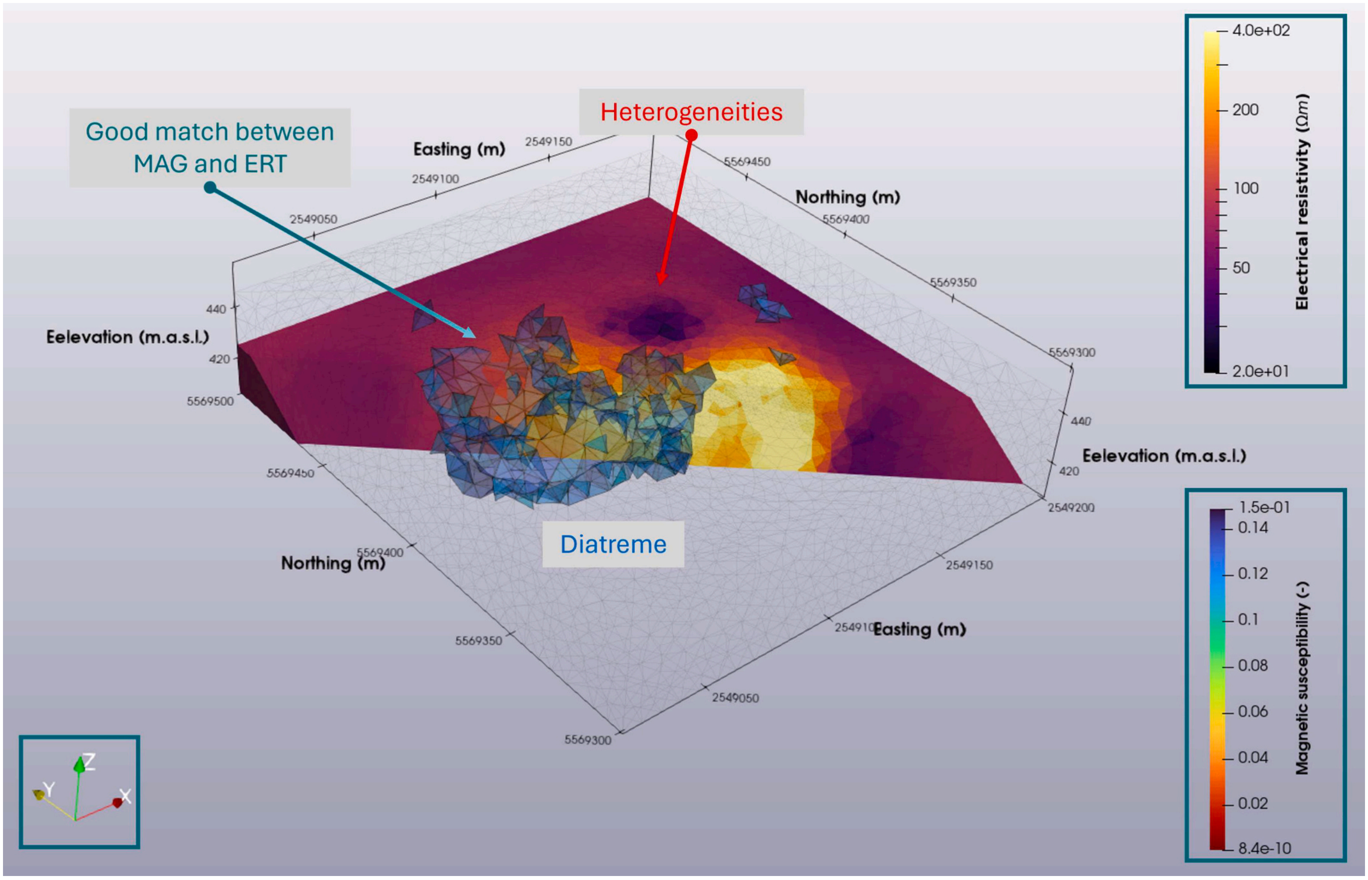

Fig. 16. 3D visualization of 3D JME ERT inversion and 3D JME magnetics (MAG) inversion.
The magnetic anomaly is shown as the blue partially transparent volume. The 3D electrical resistivity volume is sliced diagonally and at an elevation of 425 m.a.s.l. (For interpretation of the references to colour in this figure legend, the reader is referred to the web version of this article.)

5. Discussion

5.1. Structural coupling and sparsity

The synthetic data study and the field data application revealed that the JME constrained joint inversion can be applied to the ERT and the SRT method with additional considerations. In both cases the entropy constraints improved the multi-physical subsurface imaging. Both studies revealed that the structural coupling between the methods appears to be flexible as dominant features that are only present in one method are not enforced onto the other one.

Furthermore, when applied to the magnetic method, the approach not only significantly changes the shape of the anomaly but also decreases the sparsity of the solution, i.e. stronger anomalies with sharp boundaries are produced (Fig. 14). This might be an indication that this approach is most powerful for the magnetic method, or other potential field methods as indicated by Zhdanov et al. (Zhdanov et al., 2022), when comparing it to the ERT or the SRT method. The latter two require additional smoothing as pure damping does not suffice in the inversion, which in return counteracts the sparsity of the solution. Especially the seismic method seems not well suited for the entropy constraints as they tend to collapse high-velocity zones along raypaths, which produces inherently unphysical subsurface images. Since they resemble sharp boundaries and strong anomalies, it is not an issue with the entropy coupling as such, however, the effects of the entropy coupling through damping must be limited by smoothing in order to obtain reasonable, geologic models. This ultimately limits the applicability of the entropy constraints in the SRT inversion.

Furthermore, this study identified the reference model as very influential on the structural coupling as it defines regions in the model domain that are identified as anomalies by the JME constraints. In potential field methods, where data is inverted for material contrasts with respect to the background, homogeneous reference models of value zero are physical and reasonable, which eliminates the influence of the reference model. However, for other geophysical methods like the ERT or SRT method this is not the case and therefore the decision of a suitable reference model requires some thought. Reference models have to be as close as possible to the background and should not contain shared features that are meant to be recovered within the JME inversion. In case of SRT inversions, it was shown that a homogeneous model is generally preferred over gradient models and therefore should be considered if no prior information about the background of the subsurface is available. More beneficial reference models can be retrieved as low-dimensional model representations of the background based on standalone, namely conventional or ME, inversions offer improved control on structural coupling. This was shown for SRT method as a two-layered subsurface showed improvements in terms of subsurface imaging.

5.2. Inversion parameters

As to be expected, the inversion parameters define the final outcome of the JME inversion as they influence the appearance of the multi-physical images and the convergence of the inversion frameworks. In the entropy constrained cooperative inversion scheme that was presented in this paper, there are four parameters that govern joint inversion, namely the order q, the smoothing factor a, the regularization parameter λ and the method weighting factor w_m. These four parameters allow for fine-tuning of the structural coupling and the inversion outcome, for example setting method weighting factors based on prior knowledge about data quality. It was demonstrated that a suitable set of these parameters has beneficial effects on model reconstruction as well as data fit. No hard criteria could be established that define a suitable choice of those parameters, however, the following observations can guide the search for a suitable set of parameters: (1) The smoothing factor is essential to make the approach applicable to the SRT and ERT method and is in relation with the regularization parameter. (2) The synthetic data study indicates that a higher λ values in combination with a smaller smoothing is preferred over the opposite. (3) First-order entropy constraints appear to be more suitable for JME inversions as second-order expressions appear to be a too strong sparsity constraint that lead to ray path like artefacts in velocity models and noisy resistivity images. (4) Second-order ME constraints hold value for single-method inversions. (5) Grid searches can be used to find a good combination of λ and a.

6. Conclusion and outlook

This work demonstrated that the minimum entropy constrained inversion and joint minimum entropy constrained cooperative inversion introduced by Zhdanov et al. (Zhdanov et al., 2022) can be applied to the ERT and the SRT method. However, the approach needed to be extended by additional smoothing to ensure the applicability to those methods. The approach was further modified with an additional method weighting factor, which allows for better control on convergence and the structural coupling. It was shown that also the separate ME inversion holds considerable value for single method inversions as seen in the SRT or magnetic results and therefore could be added to the toolbox of geophysical inversion techniques. The study further indicates the importance of a proper set of inversion parameters as well as suitable reference models as they define the multi-physical images significantly. The results suggest that this approach is most beneficial for potential field methods and scenarios where an anomalous body is hosted in a relatively homogeneous or well known background as it promises improved structural coupling.

Furthermore, this work identifies some objectives for future studies and additional research to explore and optimize the method, such as: (1) A fair evaluation of approach with respect to other more established joint inversion approaches, for example the cross-gradients approach (Gallardo, 2007; Gallardo and Meju, 2004; Gallardo et al., 2005), joint total variation (Haber and Gazit, 2013) or the structurally-coupled cooperative inversion (SCCI) scheme of Skibbe et al. (Skibbe et al., 2021). (2) An application of the JME inversion to 3 or more methods. (3) Explore possibilities of combining the JME inversion with the SCCI of Skibbe et al. (Skibbe et al., 2021) through weighting of the smoothing operator in $\boldsymbol{W}_e$ based on the roughness of the models or the roughness of the JME stabilizer. This might lead to partially decoupled boundaries around shared anomalies, and therefore has the potential to create sharper boundaries. (4) Adjust and test new pseudo-probability density expressions that define the joint minimum entropy.

Author contributions

A.Z. carried out the research and took the lead in writing the manuscript. F.W. and M.B. supervised the project and contributed to the final version of the manuscript. All authors provided critical feedback and helped shape the research, analysis and manuscript.

CRediT authorship contribution statement

Anton H. Ziegon: Writing – original draft, Visualization, Validation, Methodology, Investigation, Conceptualization. **Marc S. Boxberg:** Writing – review & editing, Supervision. **Florian M. Wagner:** Writing – review & editing, Supervision, Project administration.

Declaration of competing interest

The authors declare that they have no known competing financial interests or personal relationships that could have appeared to influence the work reported in this paper.

Data availability

The data, the implementation, and scripts to reproduce the results are made available on the corresponding GitHub repository: https://github.com/ZiegAnt/Joint-Minimum-Entropy-Inversion-Paper.

Acknowledgements

We are grateful for the magnetic field data obtained from Ruhr University Bochum and many mathematical discussions with our colleague Hagen Söding. This manuscript was considerably improved thanks to the insightful comments made by Max Moorkamp and one anonymous reviewer.

References

Boxberg, M.S., Friederich, W.. Magnetic Field Measurements above a Phonolite Diatreme near Rockeskyll, West Eifel, Germany [Data set]. Zenodo. https://doi.org/10.5281/zenodo.13300945.
Dentith, Michael, Mudge, Stephen T., 2014. Geophysics for the Mineral Exploration Geoscientist. Cambridge University Press.
Gallardo, Luis A., 2007. Multiple cross-gradient joint inversion for geospectral imaging. Geophys. Res. Lett. 34 (19) https://doi.org/10.1029/2007GL030409.
Gallardo, Luis A., Meju, Max A., 2004. Joint two-dimensional dc resistivity and seismic travel time inversion with cross-gradients constraints. J. Geophys. Res. Solid Earth 109 (B3). https://doi.org/10.1029/2003JB002716.
Gallardo, Luis A., Meju, Max A., Pérez-Flores, Marco A., 2005. A quadratic programming approach for joint image reconstruction: mathematical and geophysical examples. Inverse Probl. 21 (2), 435. https://doi.org/10.1088/0266-5611/21/2/002.
Haber, Eldad, Gazit, Michal Holtzman, 2013. Model fusion and joint inversion. Surv. Geophys. 34, 675–695. https://doi.org/10.1007/s10712-013-9232-4.
Hopmann, P.M., 1914. Spuren eines Phonolithdurchbruches bei Rockeskyll in der Eifel. Zent. Mineral. Stutt. 35, 565.
Kana, Janvier Domra, Djongyang, Noël, Raïdandi, Danwe, Nouck, Philippe Njandjock, Dadjé, Abdouramani, 2015. A review of geophysical methods for geothermal exploration. Renew. Sust. Energ. Rev. 44, 87–95. https://doi.org/10.1016/j.rser.2014.12.026.
Kearey, Philip, Brooks, Michael, Hill, Ian, 2002. An Introduction to Geophysical Exploration, 4. John Wiley & Sons.
Klotzsche, Anja, Lärm, Lena, Vanderborght, Jan, Cai, Gaochao, Morandage, Shehan, Zörner, Miriam, Vereecken, Harry, van der Kruk, Jan, 2019. Monitoring soil water content using time-lapse horizontal borehole gpr data at the field-plot scale. Vadose Zone J. 18 (1), 190044.
Loke, Meng Heng, Dahlin, Torleif, 2002. A comparison of the gauss–newton and quasi-newton methods in resistivity imaging inversion. J. Appl. Geophys. 49 (3), 149–162. https://doi.org/10.1016/S0926-9851(01)00106-9.
Lowrie, William, Fichtner, Andreas, 2020. Fundamentals of Geophysics. Cambridge University Press.
Maack, Stefan, Küttenbaum, Stefan, Bühling, Benjamin, Niederleithinger, Ernst, 2022. Low frequency ultrasonic dataset for pulse echo object detection in an isotropic homogeneous medium as reference for heterogeneous materials in civil engineering. Data Brief 42, 108235. https://doi.org/10.1016/j.dib.2022.108235.
Menke, William, 2018. Geophysical Data Analysis: Discrete Inverse Theory. Academic press.
Mertes, Hubertus, 1983. Aufbau und Genese des Westeifeler Vulkanfeldes, 9. Institut für Geologie der Ruhr-Universität-Bochum.
Moorkamp, Max, Heincke, Björn, Jegen, Marion, Roberts, Alan W., Hobbs, Richard W., 2011. A framework for 3-d joint inversion of MT, gravity and seismic refraction data. Geophys. J. Int. 184 (1), 477–493. https://doi.org/10.1111/j.1365-246X.2010.04856.x.
Moorkamp, Max, Lelièvre, Peter G., Linde, Niklas, Khan, Amir, 2016. Integrated imaging of the earth: Theory and applications, 218. John Wiley & Sons.
Niederleithinger, Ernst, Abraham, Odile, Mooney, Mike, 2016. Geophysical methods in civil engineering: overview and new concepts. In: Bundesanstalt für Materialforschung und-prüfung (BAM).
Rücker, Carsten, Günther, Thomas, Wagner, Florian M., 2017. pyGIMLi: an open-source library for modelling and inversion in geophysics. Comput. Geosci. 109, 106–123. https://doi.org/10.1016/j.cageo.2017.07.011.
Shannon, C.E., 1948. A mathematical theory of communication. Bell Syst. Tech. J. 27 (3), 379–423. https://doi.org/10.1002/j.1538-7305.1948.tb01338.x.
Skibbe, Nico, Günther, Thomas, Müller-Petke, Mike, 2021. Improved hydrogeophysical imaging by structural coupling of 2d magnetic resonance and electrical resistivity

tomography. Geophysics 86 (5), WB77–WB88. https://doi.org/10.1190/geo2020-0593.1.

Steiner, Matthias, Wagner, Florian M., Maierhofer, Theresa, Schöner, Wolfgang, Orozco, Adrián Flores, 2021. Improved estimation of ice and water contents in Alpine permafrost through constrained petrophysical joint inversion: the Hoher Sonnblick case study. Geophysics 86 (5), WB61–WB75. https://doi.org/10.1190/geo2020-0592.1.

Wagner, Florian M., Uhlemann, Sebastian, 2021. An overview of multimethod imaging approaches in environmental geophysics. Adv. Geophys. 62, 1–72. https://doi.org/10.1016/bs.agph.2021.06.001.

Zhdanov, Michael S., 2015. Inverse Theory and Applications in Geophysics, 36. Elsevier.

Zhdanov, Michael S., Xiaolei, Tu, Čuma, Martin, 2022. Cooperative inversion of multiphysics data using joint minimum entropy constraints. Near Surf. Geophys. 20 (6), 623–636. https://doi.org/10.1002/nsg.12203.